Ocean Engineering 286 (2023) 115681

Contents lists available at ScienceDirect

Ocean Engineering

journal homepage: www.elsevier.com/locate/oceaneng

Numerical study of wave-ice floe interactions and overwash by a meshfree particle method

Ruosi Zha [a], Weiwen Zhao [b], Decheng Wan [b,*]

[a] School of Ocean Engineering and Technology, Sun Yat-sen University & Southern Marine Science and Engineering Guangdong Laboratory (Zhuhai), Zhuhai, 519082, China
[b] Computational Marine Hydrodynamics Lab (CMHL), School of Naval Architecture, Ocean and Civil Engineering, Shanghai Jiao Tong University, Shanghai, 200240, China

ARTICLE INFO

Handling Editor: Prof. A.I. Incecik

Keywords:
Wave-ice floe interaction
Overwash
Ice floe with a hole
Moving particle semi-implicit method

ABSTRACT

The interaction between regular waves and ice floes under certain wave conditions involves overwash which is characterized by waves running up over the surface of an ice floe with large deformed free surfaces. An in-house moving particle semi-implicit (IMPS) method is employed to simulate the wave-ice floe interaction, especially for the specific behavior namely overwash due to a small freeboard of sea ice and a large body motion. In this work, a series of regular waves are generated using the Lagrangian particle method based on the Stokes wave theory. Models of the floating sea ice are simplified as circular disks without and with an edge barrier and a circular disk with a central hole, which can be used to study the influences of overwash. Hydrodynamic responses of the ice floe in regular wave conditions with different wave lengths and a constant wave height are analyzed. Compared with the mesh-based methods, the Lagrangian particle-based methods have advantages in treating highly deformed free surfaces during wave overwash processes. A piston-type wave maker and a sponge layer are applied for generating waves and avoiding the wave reflection from wall boundaries, respectively. Validations are presented including the circular ice floe with a diameter of 400 mm and a thickness of 15 mm interacting with regular waves with the wave length λ/D from 1.5 to 3.5. RAOs of the original circular disk are compared with those of the circular disks with an edge barrier and with a central hole. Overwash on the ice floe can be prevented by using an edge barrier. A new type of overwash which waves flow over the upper surface and then into the hole was proposed and simulated. The present results of numerical predictions are in good agreement with the experimental data and the published numerical results using the CFD code Flow-3D.

1. Introduction

The development of trans-Arctic shipping routes and arctic engineering has attracted much attention in recent decades. Against the background of global warming, the reduction of sea ice extent in the arctic region takes place continually. It is important to study the interactions between waves and sea ice, which can be extensively observed in the transition between the open ocean and level ice coverage, i.e., the marginal ice zone (MIZ) (Lee et al., 2012; Thomson and Rogers, 2014; Huang et al., 2019). The interaction between waves and sea ice floes belongs to a very complicated phenomenon. Waves have a detrimental impact on the evolution of sea ice extent (Kohout et al., 2014). In the MIZ, the waves can lead to a movement of a solitary ice floe and collision of a group of ice floes and other coupled behaviors (Martin and Becker, 1987). The wave effect on pancake-ice dynamics has been studied (Hopkins and Shen, 2001; Dai et al., 2004; Pitt et al., 2022).

Overwash refers to an event that incident waves flow over the upper structure surface and turbulent shallow-water bores could occur which propagate along the body surface (Neli et al., 2020). Despite that extreme weather events can easily lead to overwash, for mild wave conditions with small incident amplitude or steepness, overwash could take place if the floating plate has a small freeboard. Wave overwash of ice floes is an important process that water waves wash over the surface of sea ice floes in the MIZ. Owing to the continual interactions between ocean waves and sea ice floes, there could exist waves running over the upper surface of the ice floe with a small freeboard (Matias et al., 2012). As a form of green water, overwash can be influenced by both various

* Corresponding author.
E-mail address: dcwan@sjtu.edu.cn (D. Wan).

https://doi.org/10.1016/j.oceaneng.2023.115681
Received 28 March 2022; Received in revised form 14 August 2023; Accepted 20 August 2023

wave conditions and sea ice characteristics, including wave height, wave length, ice concentration, ice thickness, ice freeboards, etc. For example, thin and fragmented ice floes are much more susceptible to wave overwash. In addition, the incident wave transmission can be attenuated due to the wave-energy dissipation caused by wave overwash and translational and rotational motions of ice floes (Toffoli et al., 2015; Montiel et al., 2016; Squire, 2020). Overwash can directly affect the mechanical behaviors of sea ice, including ice drift patterns, ice strength and deformation, ice floe mobility, ice-ice collisions, etc. During overwash, the surge of water can flow over ice floes and then flood the ice pack. As a result, wave overwash potentially changes the kinematics and dynamics of the overall ice cover in oceans. Wave overwash also has an influence on ice floe thickness by scouring, slamming, and recombination of cracked ice. Wave overwash can also affect the albedo of the ice surface, which is related to the absorption of solar radiation. Different melting rates could be obtained for the ice floes with and without wave action (Massom and Stammerjohn, 2010). It is therefore significant to study the mechanism and consequences of wave overwash of ice floes.

Wave overwash of ice floes including motion responses of thin plates with various material attributes and rigidity and wave-energy dissipations due to overwash has been studied by experimental tests and numerical simulations. Motion responses of the ice floe under the influence of wave overwash have raised important concerns. Bennetts and Williams (2015) presented experimental studies of a single thin floating disk and arrays of multiple disks interacting with incident waves. Wave energy transmissions were discussed with various wave amplitudes and frequencies for the low-concentration and high-concentration array of floating disks. The overwashed flow generated an extra load on the disk surface which led to a suppression of translational motions but an enhancement of pitch motions. This conclusion was consistent with the experimental results by McGovern and Bai (2014). Yiew et al. (2016) conducted wave basin experiments to study the wave-ice interactions by simplifying the ice as circular disks. In this work, the regular incident waves with a range of wave amplitudes and frequencies as well as the disk geometry with and without an edge barrier were discussed. The relations between surge, heave, pitch RAOs and wave parameters were analyzed for various ice floe models. Conclusions were drawn that the overwash was more likely to occur in the conditions with short wavelengths or large wave steepnesses. It was found that the motion RAOs of the disk without the presence of the edge barrier were slightly smaller than those of the disk with a barrier particularly in short waves, which meant motion responses can be suppressed by wave overwash. When a barrier was used, overwash was then prevented and motion RAOs of the disk were insensitive to incident steepness.

Another concern of overwash is the wave-energy dissipation due to wave overwash and its impacts on wave transmission. Experimental studies of transmissions and reflections of regular incident waves by a thin plastic plate were carried out by Nelli et al. (2017) in a wave flume. the impacts of drift and overwash on reflection and transmission were analyzed by employing three configures including the moored plastic sheet with barriers, the moored one without barriers and the unmoored one which was free to drift. Strong overwash of the plates without barriers for steep incident waves was observed and wave breaking in the overwash region was assumed to lead to the attenuation of wave amplitude by wave energy dissipation, especially in the rear (transmitted) field. The regular wave transmissions with the influence of overwash and wave breaking were experimentally studied by Bennetts et al. (2015). The relationship between the transmitted wave by a solitary square plastic plate and the incident wave steepnesses were analyzed. The increasing overwash depths led to an irregular transmitted wave field. For numerical simulations, a linear transmission model can be employed to predict transmission coefficients for the plate with a barrier accurately, while the results were overpredicted for a large incident steepness if overwash occurred and bores generated at the front and rear ends of the plate collide (Toffoli et al., 2015). However, overwash is not included in linear/weakly-nonlinear models. To solve this problem, overwash depths can be predicted by using a free surface above the plate ends and the nonlinear shallow water condition of overwash can be satisfied (Skene et al., 2015a, 2015b). Despite of the success of potential flow theory in solving seakeeping problems, numerical simulations by using the computational fluid dynamics (CFD) approach have been extensively developed to solve the problems of critical nonlinear flows including overwash and structures with more complex geometries. A single-phase incompressible Navier–Stokes model was developed by Orzech et al. (2016) to capture the highly nonlinear process of overwash. Two-phase model was established by Nelli et al. (2020) to simulate water motions around the plate, combined with a higher order spectral (HOS) method to simulate incident waves to reduce computational cost. The decrease of wave transmitted by the thin plate was validated with the increase of incident wave steepness. The incident wave energy was dissipated due to the process of overwash in transmitted fields.

Despite that interactions between waves and the intact floating disks have been continually studied (Li et al., 2022), it is important to investigate wave overwash of the ice floe with holes since ice floes in nature are not always intact. An ice cover can melt into many ice floes floating on the water surface due to a variety of processes including wave-ice interaction and human activities (Thomson et al., 2013). The ice hole can be generated by collision between ice and ice/marine creatures, slamming, wave impact, bubbles, etc. A hole or holes can definitely change the mass distribution, stiffness, and damage patterns of the ice. More importantly, a local free surface inside the ice can be generated (Ni et al.), which could lead to distinct motion responses and flow fields involving a new type of overwash for the wave-ice floe interactions.

Recent studies on wave-ice floe interactions are carried out by using experimental techniques, theoretical solutions and numerical simulations. For example, the flexural motion responses of the ice floe which was modeled as floating thin plastic disks were experimentally investigated by Montiel et al. (2013a, b) in a wave tank. In their model tests, the effects of the parameters were addressed involving a range of disc thicknesses, incident wave steepnesses, frequencies, etc. McGovern and Bai (2014) conducted the experiments on regular and irregular waves driven impact of sea ice floes on a circular cylinder. A series of experiments on wave-induced motions of a solitary ice disk floating on the water were carried out by Meylan et al. (2015). A barrier around the edge of the ice disk was used to prevent wave overwash. Varying wave lengths were studied to understand the wave scattering and its influences on the motion amplitudes of the disk. Huang et al. (2022) conducted experiments of surface waves around a novel model of the ice floe in a wave flume. For the structural geometry, the ice floe was composed of three layers of elastic plates. The increases of the wave steepness led to a higher overwash height over the ice floe.

Theoretical solutions for wave-ice floe interaction were pioneered by Meylan and Squire (1994) to solve the response of a solitary ice floe in ocean waves and a linear wave transmission model was proposed. In the work of Skene et al. (2015b), overwashed fluid is modeled by using the nonlinear shallow-water equations. Skene et al. (2018) studied the water wave overwash of a step using the combined potential-flow and thin-plate theories with the assumption of linear motions. However, it is difficult to deal with the coupling of overwash and the flow field around the ice floe with highly non-linearity.

Wave-induced motion responses of a floating body were mostly studied by the mesh-based CFD method (Shen et al., 2014) and the volume of fluid (VOF) method was commonly used for capturing the free surface (Zhang et al., 2019). A similar phenomenon, i.e., the green water, has been widely investigated using the CFD method (Rosetti et al., 2019; Teng et al., 2020). Based on these applications, the CFD technique can provide a novel and efficient tool to study the interaction of waves and ice and the details of flow fields. For example, Bai et al. (2017) adopted CFD simulations to study the kinematic response of small ice floes in regular waves with a couple of wave lengths and

validated the numerical results using experimental data. The results indicated the significance of considering fluid viscosity in simulating the interaction between waves and ice floes. Nelli et al. (2020) numerically studied the waves overwashing a thin floating plate, in which the linear relationship between the transmitted and incident amplitudes for thick plates was established and the decrease of the incident-wave transmission was caused by wave-energy dissipation in the overwash (Toffoli et al., 2015). Marquart et al. (2021) studied the mobile ice floes surrounded by grease ice in the MIZ and their interactions with waves on a fine scale by applying a CFD model. The shape and size of the ice floe mostly affected the strain rate and viscosity for the wave-ice interaction dynamics.

Compared with the grid-based CFD methods, Lagrangian particle-based meshless methods (Luo et al., 2021) have distinct advantages in treating the large motions of a floating body and highly deformed free surface such as overwash. For example, Zhang et al. (2019) developed and applied a Smoothed Particle Hydrodynamics (SPH) method to simulate the wave-ice interactions. An improved fluid-ice interface treatment was developed for the contact between the fluid and ice particles. The wave–ice interaction processes including the kinematic response and the flexural motion of a sea ice floe were analyzed. Tran-Duc et al. (2020) studied the motion of a flexible elastic plate under wave action by the SPH method. The results showed that the consideration of a flexural motion for an elastic plate caused significantly less overwash than that which occurred for a rigid plate. Tran-Duc et al. (2023) used SPH method to study the ice melting under the impacts of water waves in which the ice was considered as flexible. Different from the weakly-compressible SPH method, the moving particle semi-implicit (MPS) method, another typical meshfree particle-based approach, is characterized for simulating incompressible fluids in which pressures are calculated by solving a pressure Poisson equation (PPE). Park et al. (2021) applied a modified MPS method to simulate the three-dimensional nonlinear free surface flow around an advancing ship and a wedged body. Furthermore, the hybrid method combined the meshfree method and the grid-based method has been developed to simulate the waver-structure interaction. For example, the MPS-FEM coupled method was developed by Zhang et al. (2019) to study the interaction between a regular wave and a horizontal suspended structure. However, due to the shortcoming of time-consuming, most studies by using the MPS method are limited to two-dimensional simulations. Recently, the MPS-DEM method has been developed to study the wave-ice interactions and collisions among ices can be simulated based on Lagrangian particles (Amaro et al., 2022).

In this study, the in-house MPS (IMPS) method was employed to three-dimensional simulations of wave-ice floe interactions and the phenomenon of overwash. The detailed improvements of IMPS developed by our research group is summarized (Xie et al., 2022), including the improved kernel function (Zhang et al., 2014), the improved method for the free surface detection (Zhang et al., 2014), the improved discretization of the gradient operator (Lee et al., 2011), the improved format of pressure Poisson equations with a mixed source term (Lee et al., 2011), and the development of wave flume including wave making and absorbing for the linear wave and the 2nd order Stokes wave (Zhang and Wan, 2017). In this paper, we mainly focused on a three-dimensional numerical tank with meshless particles with the wave making and wave absorbing, 6-DoF body motion, which further validate the effectiveness of the original solver to solve the problems of the wave-structure interactions.

A numerical wave flume was developed to generate regular waves with varying wave lengths and a constant wave amplitude by a piston-type wave maker. Three types of ice floe geometries are studied including the circular disk, the circular disk with an edge barrier, and the circular disk with a central hole. An ice floe in seas is simplified as a thin plate. To address the effect of overwash, an edge barrier attached to the circular disk is used to increase the freeboard and therefore prevent the wave overwash. The central hole on the circular disk is designed to study various types of overwash as well as the overwash extent. This study is motivated by these typical geometries, which could behave differently from those ice floes without an edge barrier or without a central hole, especially in short wave conditions. Validations of wave generation were firstly carried out. Afterward, the surge, heave, and pitch motions of the ice floe as a circular disk, the circular disk with an edge barrier and the circular disk with a central hole are predicted. It was followed by the analysis of overwash performance for the three kinds of ice floes in waves. A novel type of overwash was discussed since the overwash waves can flow into the ice hole and interact with the local free surface inside the hole. The numerical results by the present MPS method are validated in comparison with the experimental data provided by Yiew et al. (2016) and the CFD results by Huang and Thomas (2019).

2. Mathematical model and numerical method

2.1. Governing equations

For viscous incompressible fluids, the governing equations namely the Navier-Stokes (N–S) equations including the continuity equation and the momentum equations based on Lagrangian description are written as:

$$\nabla \cdot \boldsymbol{V} = 0 \tag{1}$$

$$\frac{D\boldsymbol{V}}{Dt} = -\frac{1}{\rho}\nabla P + \nu\nabla^2\boldsymbol{V} + \boldsymbol{g} \tag{2}$$

where $\boldsymbol{V}$, t, ρ, P, ν and $\boldsymbol{g}$ represent the velocity vector, time, density of fluid, pressure, kinematic viscosity of fluid and the gravitational acceleration, respectively. Note that the governing equations are solved only for a single-phase flow, i.e., the liquid phase, in the present studies.

2.2. Particle interaction models

The kernel function proposed by Koshizuka and Oka (1996) in the original MPS method and that presented by Zhang et al. (2014) are written as follows:

$$W(r) = \begin{cases} \dfrac{r_e}{r} - 1 & 0 \le r < r_e \\ 0 & r_e \le r \end{cases} \tag{3}$$

$$W(r) = \begin{cases} \dfrac{r_e}{0.85r + 0.15r_e} - 1 & 0 \le r < r_e \\ 0 & r_e \le r \end{cases} \tag{4}$$

where r_e and r denote radii of the interaction region and the distance between particle i and particle j. Compared with the kernel function described by Eq. (3) in the original MPS method (Koshizuka and Oka, 1996), Eq. (4) has a similar form but no singularities, which helps improve the numerical stability. Therefore, Eq. (4) is adopted as the kernel function in the in-house MPS method.

The original model for solving the pressure gradient in the original MPS method (Koshizuka and Oka, 1996) is written as:

$$< \nabla P >_i = \frac{d}{n^0}\sum_{j \ne i}\frac{P_j - P_i}{|r_j - r_i|^2}(r_j - r_i)\cdot W(|r_j - r_i|) \tag{5}$$

where d is the number of spatial dimensions, and n^0 is the initial particle number density, which is defined as the sum of kernel functions of particles within the interaction region of one particle. For incompressible fluids, n^0 has a constant value which is proportional to the fluid density. The conservation of the linear and angular momentum cannot be guaranteed, which leads to nonphysical pressure oscillations in simulations by using the original MPS method. To solve this problem,

one of the improved models for the pressure gradient is employed to ensure the conservation of momentum (Lee et al., 2011). A correction term of $2P_i$ is added in the original expression of gradient, which can be written as follows.

$$\begin{aligned} <\nabla P>_i &= \frac{d}{n^0}\sum_{j\neq i}\frac{P_j - P_i + 2P_i}{|r_j - r_i|^2}(r_j - r_i)\cdot W(|r_j - r_i|) \\ &= \frac{d}{n^0}\sum_{j\neq i}\frac{P_j + P_i}{|r_j - r_i|^2}(r_j - r_i)\cdot W(|r_j - r_i|) \end{aligned} \tag{6}$$

Based on the physical concept of diffusion (Koshizuka and Oka, 1996), Laplacian term of velocity can be derived as follows.

$$<\nabla^2 V>_i = \frac{2d}{n^0\lambda}\sum_{j\neq i}(V_j - V_i)\Big)\cdot W(|r_j - r_i|) \tag{7}$$

$$\lambda = \frac{\sum_{j\neq i} W(|r_j - r_i|)|r_j - r_i|^2}{\sum_{j\neq i} W(|r_j - r_i|)} \tag{8}$$

where λ is a parameter for error compensation.

Finally, the discretization of the gradient, divergence and Laplacian operators can be summarized as:

$$<\nabla\varphi>_i = \frac{d}{n^0}\sum_{j\neq i}\frac{\varphi_j + \varphi_i}{|r_j - r_i|^2}(r_j - r_i)\cdot W(|r_j - r_i|) \tag{9}$$

$$<\nabla\cdot\boldsymbol{\Phi}>_i = \frac{d}{n^0}\sum_{j\neq i}\frac{(\boldsymbol{\Phi_j} - \boldsymbol{\Phi_i})\cdot(r_j - r_i)}{|r_j - r_i|^2}W(|r_j - r_i|) \tag{10}$$

$$<\nabla^2\varphi>_i = \frac{2d}{n^0\lambda}\sum_{j\neq i}(\varphi_j - \varphi_i)\Big)\cdot W(|r_j - r_i|) \tag{11}$$

where φ is an arbitrary scalar function, $\boldsymbol{\Phi}$ is an arbitrary vector.

2.3. Pressure Poisson equations

The Pressure Poisson Equations (PPE) can be established by satisfying the incompressible condition of MPS method which means keeping the particle number density constant. In each time step, there are two main procedures: first, temporal velocity of particles is predicted based on viscous and gravitational forces, and particles are moved according to the temporal velocity; second, the pressure is implicitly calculated by solving a Poisson equation, and the velocity and position of particles are updated according to the obtained pressure. In the original MPS method (Koshizuka and Oka, 1996), the pressure Poisson equations are derived based on the assumption of incompressibility that the intermediate fluid density and/or the particle number density must be constant through numerical correction.

$$<\nabla^2 P^{n+1}>_i = -\frac{\rho}{\Delta t^2}\frac{<n^*>_i - n^0}{n^0} \tag{12}$$

where n^* is the particle number density in the intermediate step. However, the pressure field obtained by the original form of the PPE always suffers from oscillations both in spatial and temporal domains since the particle number density is not always smooth.

A mixed source term using the divergence of the intermediate velocity can be added in the PPE to suppress the unphysical oscillations of pressure. The PPE with a mixed source term in the present IMPS solver is derived as

$$<\nabla^2 P^{n+1}>_i = (1-\gamma)\frac{\rho}{\Delta t}\nabla\cdot V_i^* - \gamma\frac{\rho}{\Delta t^2}\frac{<n^*>_i - n^0}{n^0} \tag{13}$$

where γ is a blending parameter with a value between 0 and 1. In this paper, $\gamma = 0.01$ is adopted for all simulations according to the work of Zhang and Wan (2018).

2.4. Boundary conditions

The wall boundary conditions can be simulated by using one layer of wall particles and two layers of dummy particles distributed outside the wall boundary along with the normal directions of the wall particles. For wave generation, the wave maker is set as a moving wall boundary condition with an imposed motion. Since the pressure of a free surface particle is the same as the atmospheric pressure, the zero-pressure boundary condition is imposed on the free surface. To avoid the misidentification of the free surface particles, an improved method for the free surface detection by Zhang et al. (2014) in which a vector defined as follows:

$$<\boldsymbol{F}>_i = \frac{d}{n^0}\sum_{j\neq i}\frac{1}{|r_i - r_j|}(r_i - r_j)W(r_{ij}) \tag{14}$$

where the vector function $\boldsymbol{F}$ represents the asymmetry of arrangements of neighbor particles. The criteria for a free surface particle are determined by:

$$<|\boldsymbol{F}|>_i \; > 0.9|\boldsymbol{F}|^0 \tag{15}$$

where $|\boldsymbol{F}|^0$ is the initial value of $|\boldsymbol{F}|$ for a given surface particle in the initial field.

2.5. Wave making and absorbing

For wave making and absorbing in the present IMPS solver, a piston-type wave generator is incorporated as the wave-making boundary and a sponge layer is employed to avoid wave reflection, as shown in Fig. 1. A periodic movement is imposed to a paddle as the wave making boundary at the left end and a sponge layer is set at the right end of the wave flume to absorb waves to suppress the effect of wave reflections.

According to the linear Stokes wave theory, the free surface elevation, η, can be written as follows:

$$\eta = \frac{S}{2}\left[\frac{4\sinh^2(kh)}{2kh + \sinh(2kh)}\cos(kx - \omega t)\right] = \frac{H}{2}\cos(kx - \omega t) \tag{16}$$

where h, H, k and ω stand for the water depth, wave height, wave number, and angular frequency, respectively. S is the maximum displacement of the piston. The wave length, λ, can be obtained based on the dispersion relation:

$$gk\tanh(kh) - \omega^2 = 0 \tag{17}$$

The displacement and the velocity of the piston can be derived as follows:

$$x(t) = \frac{H}{2}\left[\frac{2kh + \sinh(2kh)}{4\sinh^2(kh)}\right]\sin(\omega t) \tag{18}$$

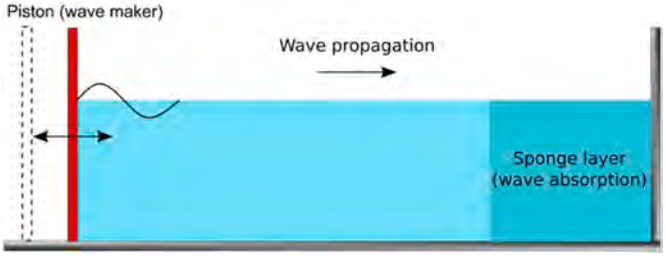

Fig. 1. The wave maker and sponge layer.

$$u(t)=\frac{H\omega}{2}\left[\frac{2kh+\sinh(2kh)}{4\sinh^2(kh)}\right]\cos(\omega t) \tag{19}$$

The motion of the particles on the boundary of wave generation can be prescribed by Eqs. (18) and (19). The 2nd order Stokes wave theory can be used to generate the regular waves with a relatively large wave amplitude. The free surface elevation was corrected according to:

$$\eta=a\cos(kx-wt)+a_{2p}\cos 2(kx-wt) \tag{20}$$

where $a=H/2$ is the wave amplitude and the corrected wave amplitude, a_{2p}, is calculated as follows:

$$a_{2p}=\frac{ka^2}{4}\frac{(2+\cosh 2\,kh)\cosh kh}{\sinh^3 kh} \tag{21}$$

The displacement of the piston can be derived as follows:

$$x(t)=\xi_0\left[\sin(\omega t)-\frac{a}{2hn_1}\left(\frac{3}{4\sinh^2 kh}-\frac{n_1}{2}\right)\sin 2\,\omega t\right] \tag{22}$$

where

$$\xi_0=\frac{an_1}{\tanh kh} \tag{23a}$$

$$n_1=\frac{1}{2}\left(1+\frac{2kh}{\sin 2\,kh}\right) \tag{24a}$$

A sponge layer is placed on the other side of the wave tank to avoid the wave reflection. In the sponge layer, an artificial damping term is added to the source term for wave absorption:

$$f_s(x)=\begin{cases}-\rho\alpha_s\dfrac{x-x_s}{L_s}u\\ 0\end{cases} \tag{25a}$$

where x_s is the horizontal coordinate of the start of the sponge layer, L_s is the total length of the sponge layer, α_s is the non-dimensional coefficient in terms of the intensity of wave absorption.

2.6. Six-DoF motions of a rigid body

The motion of a floating body is governed by the equations of rigid body dynamics, following the Newton's law of motion. The wave-induced movement of a floating body includes the coupling of translation and rotation, i.e., the surge, sway, heave, roll, pitch and yaw. Two coordinate systems including the earth-fixed and body-fixed coordinate systems are adopted to solve the six-degree-of-freedom (six-DoF) equations of motion. The procedure of solving the equations of motion of a rigid body can be summarized as follows. Firstly, the total force on the body and moment based on the mass center of the body are calculated in the earth-fixed coordinate system:

$$\boldsymbol{F}_e=(X_e,Y_e,Z_e)=m\boldsymbol{g}+\int(\tau d|\boldsymbol{S_e}|+pd\boldsymbol{S_e}) \tag{26}$$

$$\boldsymbol{M_e}=(K_e,M_e,N_e)=\boldsymbol{r}_{cg}\times m\boldsymbol{g}+\int\boldsymbol{r}\times(\tau d|\boldsymbol{S_e}|+pd\boldsymbol{S_e}) \tag{27}$$

where $\boldsymbol{F_e}$ and $\boldsymbol{M_e}$ stand for the total force exerted on the rigid body in the earth-fixed coordinate system, respectively. τ and p are the shear force and the total pressure on the body surface. $\boldsymbol{S_e}$ is the normal vector of the particle on the body surface.

Afterward, the force and moment are transferred to the local body-fixed coordinate system as $\boldsymbol{F_b}=(X_b,Y_b,Z_b)$ and $\boldsymbol{M_b}=(K_b,M_b,N_b)$ using the coordinate transformation matrix. The acceleration, velocity and displacement of the rigid body can be solved in the body-fixed coordinate system. The six-DoF equations of motion can be written as follows:

$$\begin{cases}\dot{u}=X_b/m+vr-wq+x_g(q^2+r^2)-y_g(pq-\dot{r})-z_g(pr+\dot{q})\\ \dot{v}=Y_b/m+wp-ur+y_g(r^2+p^2)-z_g(qr-\dot{p})-x_g(qp+\dot{r})\\ \dot{w}=Z_b/m+uq-vp+z_g(p^2+q^2)-x_g(rp-\dot{q})-y_g(rq+\dot{p})\\ \dot{p}=\left\{K_b-(I_z-I_y)qr-m\left[y_g(\dot{w}-uq+vp)-z_g(\dot{v}-wp+ur)\right]\right\}/I_x\\ \dot{q}=\left\{M_b-(I_x-I_z)rp-m\left[z_g(\dot{u}-vr+wq)-x_g(\dot{w}-uq+vp)\right]\right\}/I_y\\ \dot{r}=\left\{N_b-(I_y-I_x)pq-m\left[x_g(\dot{v}-wp+ur)-y_g(\dot{u}-vr+wq)\right]\right\}/I_z\end{cases} \tag{28}$$

where the subscript b represents that the force and moment are in the body-fixed coordinate system. $\boldsymbol{v}=(u,v,w,p,q,r)$ is the velocity/angular velocity in the body-fixed coordinate system. $\boldsymbol{a}=(\dot{u},\dot{v},\dot{w},\dot{p},\dot{q},\dot{r})$ is the acceleration/angular acceleration in the body-fixed coordinate system.

The obtained velocities then should be transferred to the earth-fixed coordinate system. Finally, the floating body will be moved according to its velocity and displacement in the earth-fixed coordinate system.

3. Numerical results and discussions

3.1. Parameters of the ice floe

In the present numerical simulations, the parameters of the ice floe are set from the experiments conducted by Yiew et al. (2016). The model of an ice floe can be simplified as a circular cylinder disk. The three ice floe models with different geometries, including a circular disk, a circular disk with an edge barrier and a circular disk with a central hole, are presented in Fig. 2. The edge barrier attached to the circular disk can prevent overwash water onto the upper surface of the ice and the effects of overwash can be studied by comparing the wave responses of the three ice floes. The ice model represented by a circular disk is named as Model 1, the model with an edge barrier is called Model 2 and the model but with a hole but no edge barrier is declared as Model 3 in the following sections.

The diameter and thickness of the circular ice floe without an edge barrier are D = 400 mm and t = 60 mm, respectively. Note that the thickness of the circular ice floe in the experimental tests is 15 mm. For the ice floe with an edge barrier, the diameter and thickness are the same as those of the ice floe without an edge barrier. The height and thickness of the edge barrier are $H_b=50$ mm and $t_b=25$ mm, respectively. For the ice floe with a central hole, Model 3, the diameter of the hole in the center is $D_h=200$ mm. The diameter and thickness of Model 3 are the same as those of Model 1. The density of each model is set as 636 kg/m^3. The density of the water is set as 998 kg/m^3 since it is freshwater. The ice floe is considered as a rigid body, which means the structural deformation is neglected for the present wave-ice floe interactions.

3.2. Computational set-up

The sketch of the three-dimensional computational domain, boundary conditions and the numerical wave flume with an ice floe floating on the free surface is shown in Fig. 3. The dimensions of the computational domain are defined as follows. L, W and H_d stand for the total length, width and height of the wave tank, respectively. In particular, h is the water depth, L_p is the initial distance between the wave maker (the piston) and the left boundary of the tank, L_s is the length of the sponge layer near the right boundary of the tank for wave absorbing, and L_i is the initial distance between the wave maker and the ice floe along the x-direction. These dimensions are determined as verified or acceptable values for the present studies. For example, L_p depends on the maximum displacement of the wave maker. A periodic movement along the X-direction is imposed to the piston for wave-making. The equation of displacement of the piston is given in Eq. (18). Initially (t = 0 s), the piston is located at the midline of a sinusoidal function (X = 0 m). L_p should be greater than the amplitude of the sinusoidal function, otherwise the water could leak from the left bottom. The maximum amplitude of the moving piston for all wave conditions is 0.2 m, which can be

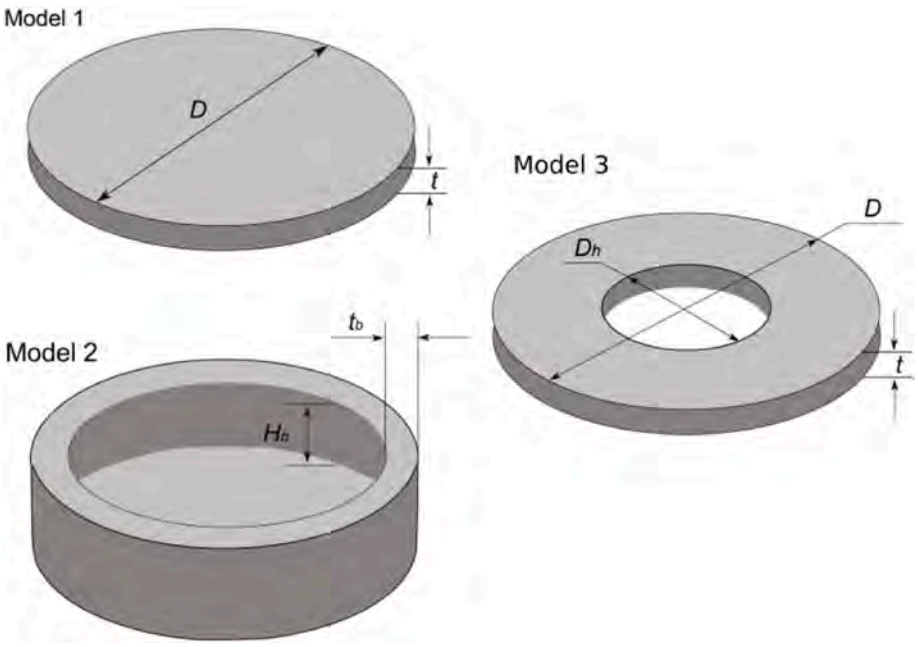

Fig. 2. Geometry of the circular disk (Model 1), the circular disk with an edge barrier (Model 2) and the circular disk with a central hole (Model 3).

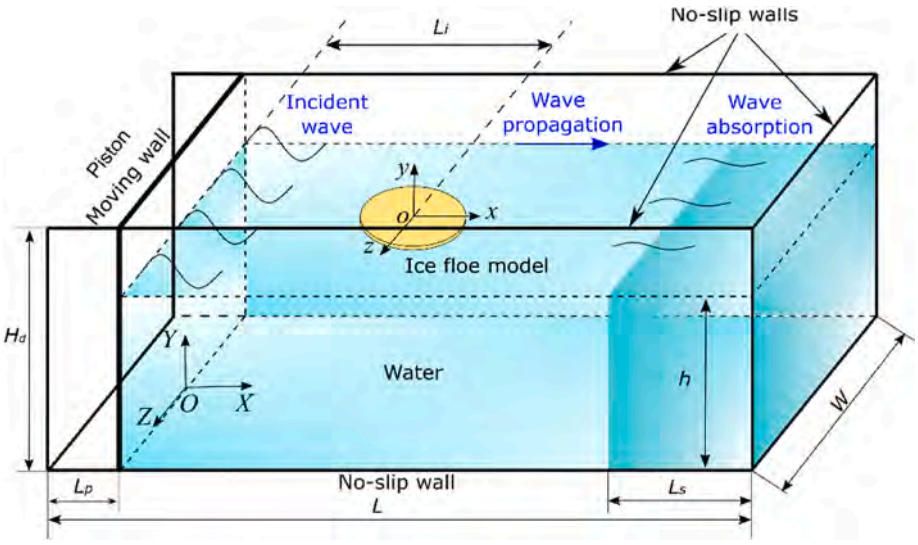

Fig. 3. Sketch of the computational domain, boundary conditions and coordinate systems.

calculated as by Eq. (18) if letting $wt = \pi/2$. Consequently, L_p is set as 0.5 m ($L_p/D = 1.25$), which is an acceptable value in this study. L_i depends on the wave length. Generally, at least one integral wave should be generated before the wave interacting with the structure. Based on the previous experience in the research of wave-structure interactions (Shen and Wan, 2013), it is usually set at least one wave length. The time history of wave elevation at L_i/D is provided to validate the effectiveness of the wave-making. In this study, an acceptable value of $L_i/D = 3.85$ is used, which is a little greater than $\lambda_{max}/D = 3.5$.

The earth-fixed coordinate system, *O-XYZ*, is built at the bottom centerline of the wave tank, while the local body-fixed coordinate system, *o-xyz*, is built at the mass center of the ice floe. Initially, the piston-type wave maker is located at $X = 0$ and the distance between initial position of the center of the ice floe and initial position of wave maker is 1.5 m. Waves propagate along the *x*-direction. The water is to a depth of $h/D = 2.075$ ($h = 0.83$ m) in the wave flume according to the experimental set-up (Yiew et al., 2016). Meanwhile, the condition of deep-water waves ($h > \lambda/2$) can be satisfied when h/D is 2.075 (if λ_{max}/D is 3.5). For the domain height, H_d, the air phase above the water is not taken into account. The value of H_d/D should be greater than $h/D = 2.075$ plus the wave height ($H/D = 0.2$), to prevent the particles on waves from moving outside. For example, $H_d/D = 2.75$ ($H_d = 1.1$ m) is an acceptable value.

Table 1
Summary of the wave conditions.

Wave length, λ/D	Wave height, H/D	Wave angular frequency, ω (rad/s)	Wave period, T_0 (s)
1.5	0.2	10.1356	0.62
1.725	0.2	9.4515	0.66
2.0	0.2	8.7777	0.72
2.5	0.2	7.8508	0.80
3.0	0.2	7.1657	0.88
3.5	0.2	6.6314	0.95

The parameters of regular wave conditions for the cases in the present simulations are summarized in Table 1. Six wave conditions are investigated with the non-dimensional wave length λ/D from 1.5 to 3.5. Note that the water depth is $h/D = 2.075$ for all cases. The wave height for all cases is set as $H/D = 0.2$. It can be calculated that the maximum wave steepness is therefore 0.13.

3.3. Validation of wave generation

Firstly, the numerical wave generation was validated for the simulations with three wave lengths ($\lambda/D = 1.5$, 2.5 and 3.5) and the same wave heights. In this case, there were no objects in the wave tank. A wave probe was placed at the location of $X = 1.5$ m, which was corresponding to the center of the circular ice floe in the following studies. For the wave condition of $\lambda/D = 2.5$, a convergence study and a temporal convergence study were carried with four sets of particle spacings and three sets of time steps, respectively. The verification results of wave elevations for the wave length of $\lambda/D = 2.5$ are shown in Fig. 4. It can be observed the numerical results converged with the decrease of the particle spacing and the decrease of the time step. The converged wave elevations were in agreement with the theoretical results. For statistical analysis, the relative errors of the wave amplitude and wave period between the numerical results and theoretical solution are given in Table 2. The relative errors for the converged results were both lower than 1%. It shows that the results obtained by the present numerical methods and parameters of settings are verified.

To verify the wave absorbing capacity, the wave condition is chosen as the wave with the maximum wave length ($\lambda_{max}/D = 3.5$). As shown in Fig. 5, three values of L_s/λ including 0.5, 0.7 and 1.0 are studied. In these cases, the value of α_s is fixed as 50. Afterward, three values of α_s including 40, 50 and 60 are investigated with a value of $L_s/\lambda = 1.0$. The relative errors in Table 2 indicated that the numerical results converged with the values of L_s/λ increased. The minimum relative errors were obtained when α_s was set as 50. Compared to the theoretical solution, the results show that $L_s/\lambda = 1.0$ and $\alpha_s = 50$ are determined as the verified value.

Consequently, a total number of 716,180 particles with a particle spacing equaling to 0.02 m was used for a balance of accuracy and the computational cost. The number of fluid particles is 550,466. The time step is set as $\Delta t = 0.001$ s for numerical stability. The numerical results of the three cases are compared with the theoretical solutions in Fig. 6. Two points of the wave flume are presented, i.e., Point 1 ($X/D = 3.75$) and Point 2 ($X/D = 7.50$). It can be observed that the numerical results with the wave lengths from $\lambda/D = 1.5$ to 3.5 calculated by the present method is close to the theoretical solutions. At the beginning stage of the curves, the water particles were accelerated and started to move under the action of the piston for wave generation. The particle velocities are then increased until the expected values based on various wave conditions are satisfied, therefore there are a segment of time series did not agree with theoretical solution at the beginning stage. Table 3 presents

Table 2
Error analysis of the wave generation for verification.

Parameters	Wave height, H/D	Relative error of wave height	Wave period, T_0 (s)	Relative error of wave period
Theoretical	0.200	–	0.800	–
$l_0 = 0.031$ m	0.074	63.1%	0.776	3.0%
$l_0 = 0.025$ m	0.182	8.9%	0.813	1.6%
$l_0 = 0.020$ m	0.198	0.8%	0.795	0.6%
$l_0 = 0.016$ m	0.203	1.4%	0.804	0.5%
$\Delta t = 1.4E\text{-}3$ s	0.043	78.6%	0.798	0.3%
$\Delta t = 1.0E\text{-}3$ s	0.198	0.8%	0.795	0.6%
$\Delta t = 0.7E\text{-}3$ s	0.191	4.7%	0.802	0.2%
Theoretical	0.200	–	0.950	–
$L_s/\lambda = 0.5$	0.194	2.9%	0.961	1.2%
$L_s/\lambda = 0.7$	0.205	2.6%	0.943	0.7%
$L_s/\lambda = 1.0$	0.199	0.7%	0.943	0.7%
$\alpha_s = 40$	0.214	6.9%	0.960	1.1%
$\alpha_s = 50$	0.199	0.7%	0.943	0.7%
$\alpha_s = 60$	0.186	7.0%	0.948	0.2%

the relative errors of the wave elevations at two points between the numerical results and the theoretical solutions. The errors of the wave height at Point 1 (P1) were small while those at Point 2 (P2) were relatively large especially for short waves. The error could be resulted from the numerical dissipation during wave propagating from P1 to P2. Generally, wave generations can be validated by using the present numerical methods. It is indicated that the energy conservative of simulations using the IMPS method is good for the wave ($\lambda/D = 2.5$), and acceptable for $\lambda/D = 1.5$ and $\lambda/D = 3.5$ under the limitation of particle-based methods. The discrepancy of the wave amplitude against the theoretical solution is generally less than the particle spacing employed in each case. The discrepancies between the numerical wave profile and the theoretical values could be caused by the following reasons. Firstly, the accuracy of wave probes can affect the results of wave profiles. To solve this problem, the average coordinate of two particles is adopted as the wave elevation at the point of wave probe. These two particles are determined as the nearest particle located at the left side and right side, respectively. Due to the dissipated energy, the wave amplitude for the short wave is smaller than the theoretical solution. More particles with smaller particle spacings could be used to decrease the discretization error. However, it will extremely increase the computational cost.

Therefore, the present meshfree method is validated for wave generation. As an example, the free surface at $t = 7.0$ s and $t = 7.4$ s is shown in Fig. 7. It can be observed that the wave elevations in the wave absorption zone tend to be the initial water depth. In a summary, the wave

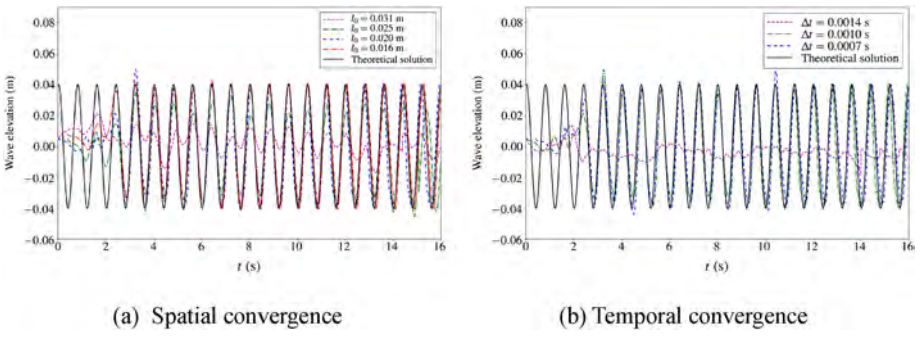

(a) Spatial convergence (b) Temporal convergence

Fig. 4. Spatial and temporal convergence studies of wave elevations at $X/D = 2.75$ ($\lambda/D = 2.5$).

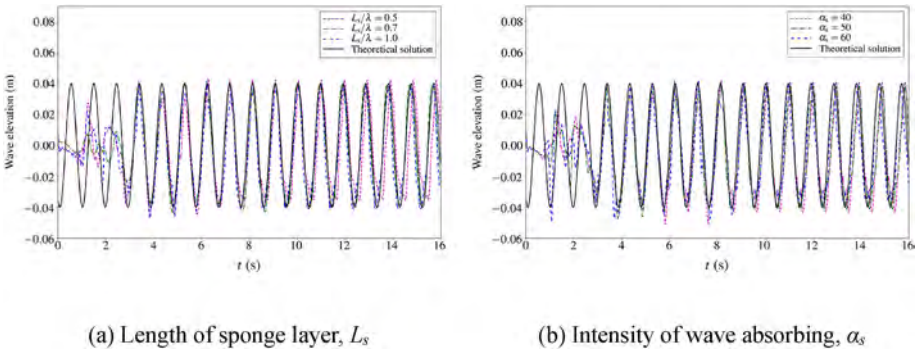

Fig. 5. Convergence studies of wave absorbing parameters at $X/D = 3.75$ ($\lambda/D = 3.5$).

generation and absorption by the present method can be applied to study the interactions between waves and the ice floe in the following studies.

3.4. Wave interacting with an ice floe

The wave-ice floe interaction was then simulated by applying three sorts of the ice floe, involving Model 1, Model 2 (with an edge barrier) and Model 3 (with a central hole). The wave conditions are the same as the cases given in Table 1. Three degrees of freedom, i.e., the surge, heave and pitch, are investigated for wave-induced movement of the ice floe. In the body-fixed coordinate system, the surge and heave are translational motions along the *x*-axis and *y*-axis while the pitch is a rotational motion along the z-axis. The motions of the other three degrees of freedom, involving the sway, roll and yaw, are fixed in this study. Note that the surge motion is a superposition of a harmonic oscillation and a steady drift due to the incoming wave celerity. The response amplitude operators (RAOs) for surge, heave and pitch motions can be calculated by:

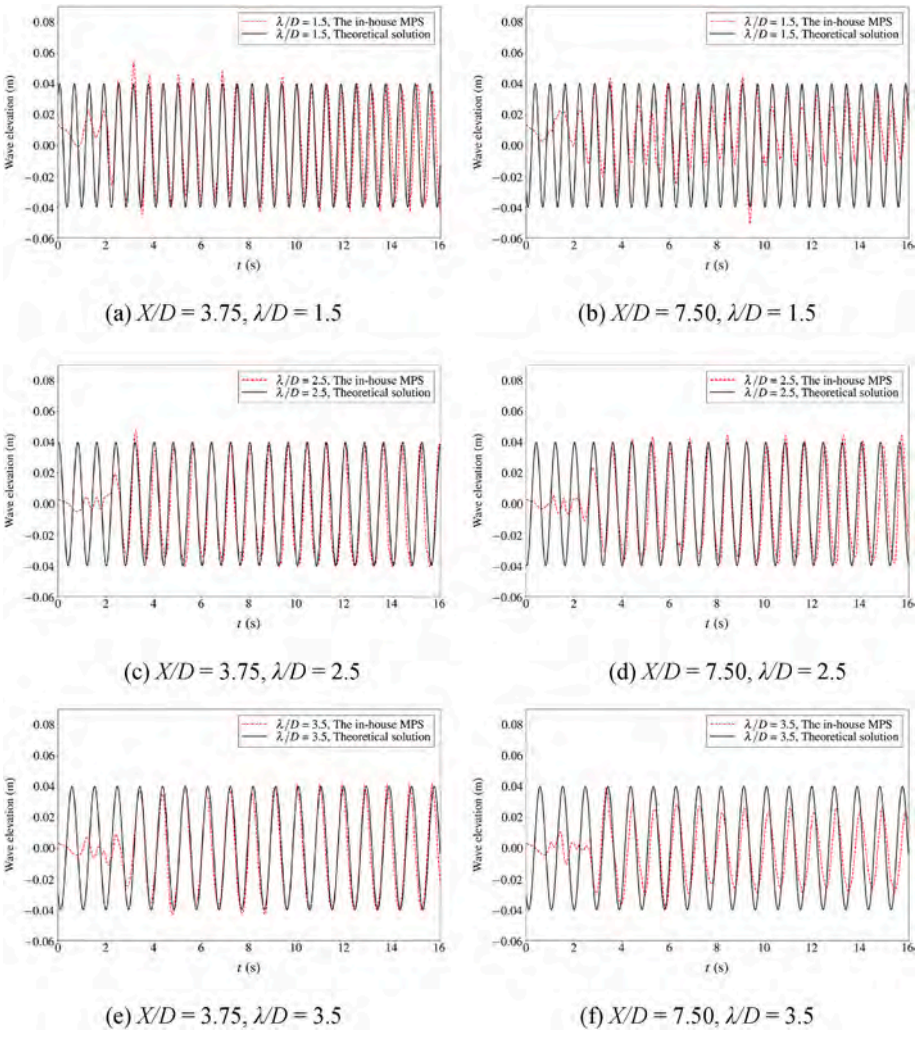

Fig. 6. Time histories of wave elevations at two points of the flume for validation.

Table 3
Error analysis of the wave elevations at two points for validation.

Items	Wave height, H/D	Relative error of wave height	Wave period, T_0 (s)	Relative error of wave period
Theoretical	0.200	–	0.620	–
P1 ($X/D = 3.75$)	0.207	3.5%	0.625	0.8%
P2 ($X/D = 7.50$)	0.118	40.9%	0.623	0.4%
Theoretical	0.200	–	0.800	–
P1 ($X/D = 3.75$)	0.198	0.8%	0.795	0.6%
P2 ($X/D = 7.50$)	0.207	8.9%	0.805	0.6%
Theoretical	0.200	–	0.950	–
P1 ($X/D = 3.75$)	0.204	2.1%	0.943	0.8%
P2 ($X/D = 7.50$)	0.136	31.9%	0.963	1.3%

$$\mathrm{RAO}_{surge} = \frac{a_s}{a\coth(kh)} \tag{23b}$$

$$\mathrm{RAO}_{heave} = \frac{a_H}{a} \tag{24b}$$

$$\mathrm{RAO}_{pitch} = \frac{a_P}{ka} \tag{25b}$$

where a is the wave amplitude, k is the wave number and h is the water depth, respectively. a_S, a_H and a_P are the amplitude of surge after eliminating the drift value, the amplitude of heave and the amplitude of the pitch angle, respectively. In this work, three periods of motions were adopted to calculate the mean values to decrease the errors consequently.

Convergence studies on the domain length and domain width are carried out to verify the dimensions and resolutions in the present IMPS simulations. For the case of ice floe (model 2) in the wave with $\lambda/D = 2.5$, the wave elevations at $X/D = 5.75$ in the wake of the ice are compared. Three values of the domain length including $L/D = 12$, 15 and 18 and three values of the domain width, i.e., $W/D = 2.5$, 3.0 and 3.5 are investigated. The wave elevations at the wave probe are shown in Fig. 8(a) and (b). It was assumed that the results of the largest domain length and domain width will be the exact value. The relative errors of the wave height calculated by the in-house MPS solver are given in Table 4. It is indicated that the numerical results are converged when the domain length/width is increased. Since the difference between the result of $L/D = 15$ and 18 is small, the domain length was determined as $L/D = 15$ to save the computational cost. The domain width was set as $W/D = 3.5$ to decrease the wall effects in the following studies.

Based on the results of convergence studies, a particle spacing of 0.02 m and a time step of 0.001 s were used for simulating waves interacting with an ice floe. A total number of 984,691 particles for the cases with Model 1 and 985,032 particles for the cases with Model 2 were generated accordingly. The number of solid particles of Model 1 was 1,023 and that of Model 2 was 1,364. For all cases, the number of fluid particles was kept the same as 793,354. Since the three-dimensional simulations are very time-consuming, parallel computations on high performance computers based on MPI method are carried out to improve the numerical efficiency. The CPU used for the present simulations was Intel(R) Xeon(R) CPU E5-2697A v4 with 32 processors. For each case, a total of 55 h per case were consumed for the current 3-D computations with a physical time of up to 16 s.

The time series of the surge, heave and pitch under three wave conditions are shown in Fig. 9. It shows that after the wave profile is

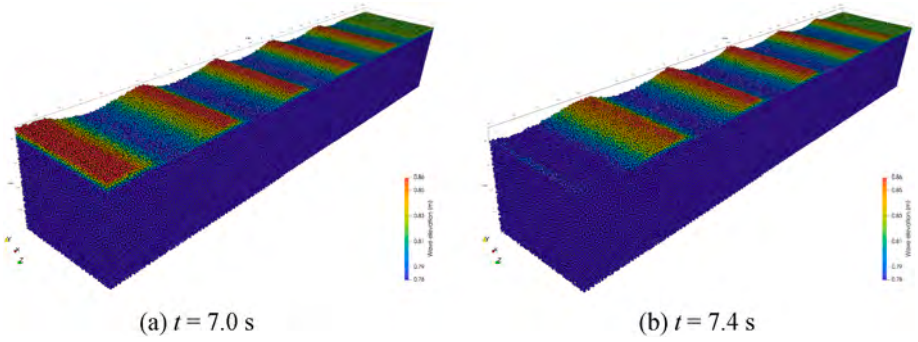

Fig. 7. Free surface for the wave with $\lambda/D = 2.5$ at (a) $t = 7.0$ s and (b) $t = 7.4$ s.

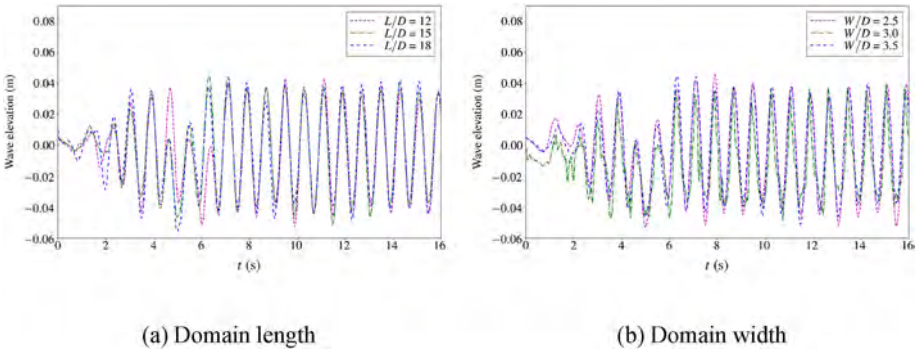

Fig. 8. Convergence studies of wave elevations at $X/D = 5.75$ (λ/D = 2.5).

Table 4
Error analysis of effects of domain size on wave elevations.

Domain size	Wave height, H/D	Relative error of wave height
$L/D = 18$	0.233	–
$L/D = 15$	0.233	0.2%
$L/D = 12$	0.228	2.3%
$W/D = 3.5$	0.228	–
$W/D = 3.0$	0.238	4.4%
$W/D = 2.5$	0.213	6.6%

steady, there are more than three cycles of harmonic response are available for the analysis in the frequency domain, and the RAOs of motions can be calculated based on the first-order amplitude.

The numerical results of RAOs for the surge, heave and pitch under six wave conditions for Model 1 and Model 2 are presented in Figs. 10 and 11, respectively. The results calculated by the in-house MPS method (denoted by the blue circles) were compared with those by the experimental data (denoted by the black crosses) and the numerical results by the CFD software Flow-3D (denoted by the red dash lines) by Huang and Thomas (2019). Note that experimental results were only available for the last two wave lengths ($\lambda/D = 2.5$ and 3.5).

For Model 1 without an edge barrier and without a hole, RAOs for the surge are in good agreement with the experimental data and the numerical results by Flow-3D as shown in Fig. 10(a). Against the experimental data, the two numerical results are generally overpredicted for all the six wave lengths. As shown in Fig. 10(b), the RAOs for the heave agree well with the experimental data and the numerical results by Flow-3D for all wave lengths, λ/D from 1.5 to 3.5. The RAOs for the heave by the present method are closer to the experimental data for the wave length of $\lambda/D = 2.5$ but overpredicted for $\lambda/D = 3.5$. RAOs for the pitch shown in Fig. 10(c) indicate agreement for all wave lengths. However, discrepancies existed for the present results with overprediction for the wave length of $\lambda/D = 2.0$, 2.5 and 3.5. The comparison of the RAOs for the surge of Model 2 with an edge barrier is similar to that for Model 1 as shown in Fig. 11(a). In terms of the RAOs for the heave of Model 2 in Fig. 11(b), the results by MPS method and by Flow-3D are both overpredicted against the experimental data for the wave length of $\lambda/D = 2.5$. For the case with a wave length of $\lambda/D = 3.5$, both numerical results are in good agreement with the experimental data. As shown in Fig. 11(c), the RAOs for the pitch obtained by MPS method agree better than those by Flow-3D against the experimental data for the wave length of $\lambda/D = 2.5$. The two numerical results are predicted well for the wave length of $\lambda/D = 3.5$. In a summary, the results in the present work generally agreed well with the published numerical results (Huang and Thomas, 2019) and the experimental data (Yiew et al., 2016). The RAOs for the surge, heave and pitch of Model 3 with a hole are compared with the numerical results of Model 1 and Model 2 in Fig. 12. The results suggest that the motion responses of the ice floe could be affected by the edge barrier and the hole. For example, the RAOs for Model 2 are higher than those for the Model 1 and Model 3 for the cases with the wave length λ/D from 1.5 to 2.0. Overwash occurred frequently within this particular range of wave length. In addition, for the wave length greater than 2.0, i.e., from 2.5 to 3.5, the RAOs for those three models are generally close since no overwash was observed. For Model 3 with a hole, the RAOs are smaller than those for Model 1 with no holes for the cases with the wave length λ/D from 1.5 to 2.0, while the results are a

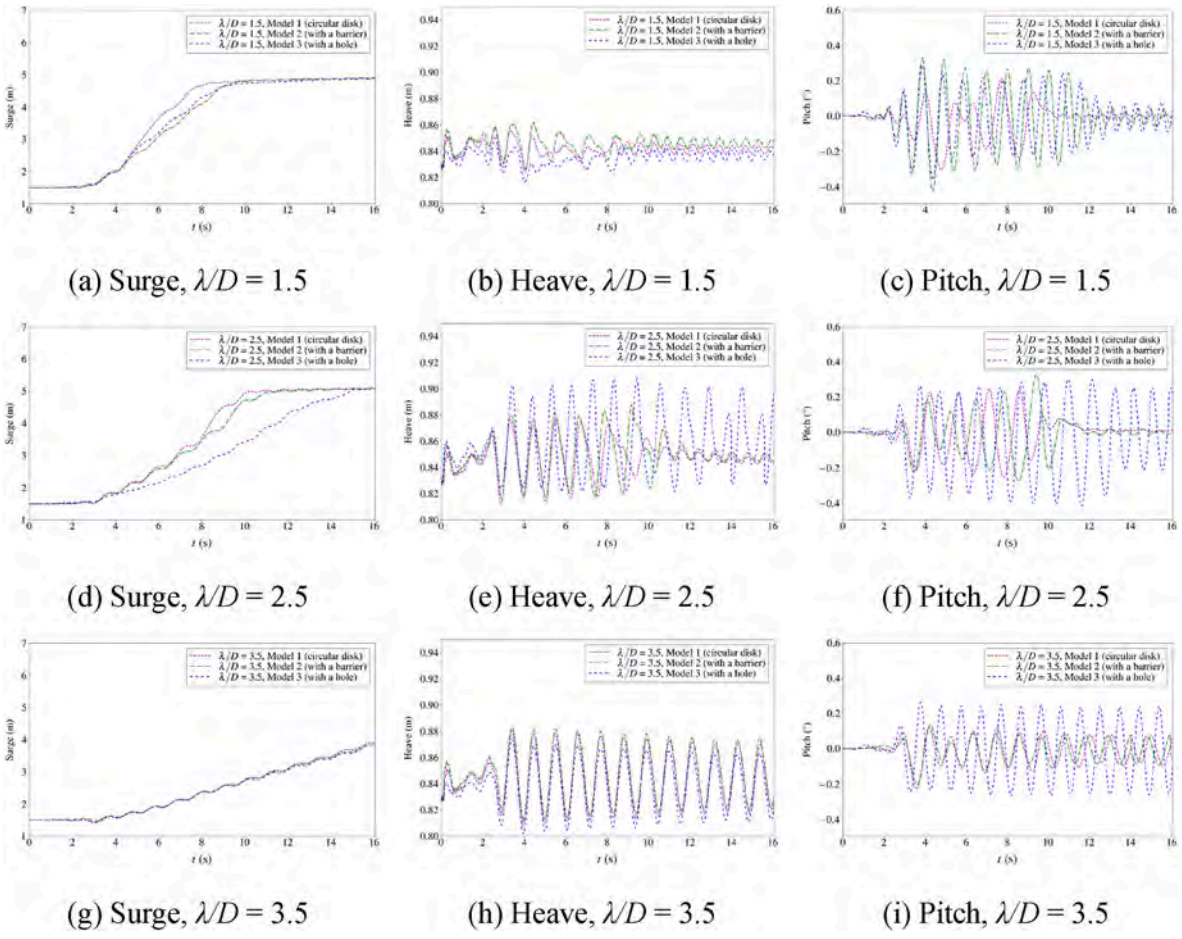

Fig. 9. Time series of the surge, heave and pitch motions of three ice floes.

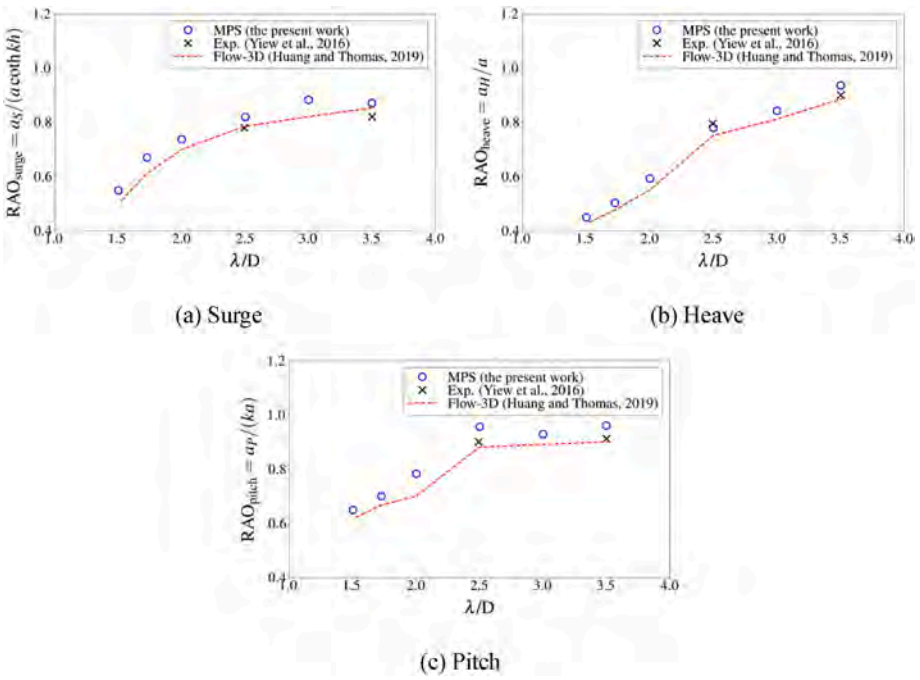

Fig. 10. Comparison of RAOs for Model 1.

little greater for the cases with the wave length λ/D from 2.5 to 3.5. It can be concluded that the effects of overwash can suppress the body motion of the ice floe.

Overwash was observed for the wave condition with a small wave length and high wave steepness. Four typical instants of the free surface with a contour of wave elevation for Model 1 with no edge barrier at the wave length of $\lambda/D = 1.5$ are shown in Fig. 13.

The ice floe disk drifted towards the x-axis due to the surge motion. It can be seen that the flow field around the ice floe interfered with overwash waves. It can be concluded that the overwash waves with a highly deformed free surface can be well simulated by the present MPS method. It is indicated that overwash occurred mainly due to two reasons. First, the freeboard of the ice floe is very small especially when the disk is very thin. The freeboard of the ice floe is always smaller than the wave amplitude in the present studies. Therefore, waves are likely to flow over the upper side of the ice floe. Another factor is the wave-induced motion of the ice floe, including the heave and pitch. When the ice floe is tilted with a pitch angle, it could have emerged into the water and overwash could be more likely to happen. The comparison of overwash in a local view for the three ice floe models, Model 1, Model 2 and Model 3 in the given waves with $\lambda/D = 1.5$ and $\lambda/D = 3.5$ are presented in Fig. 14, respectively. The snapshots at $t = t_0$ and $t = t_0$

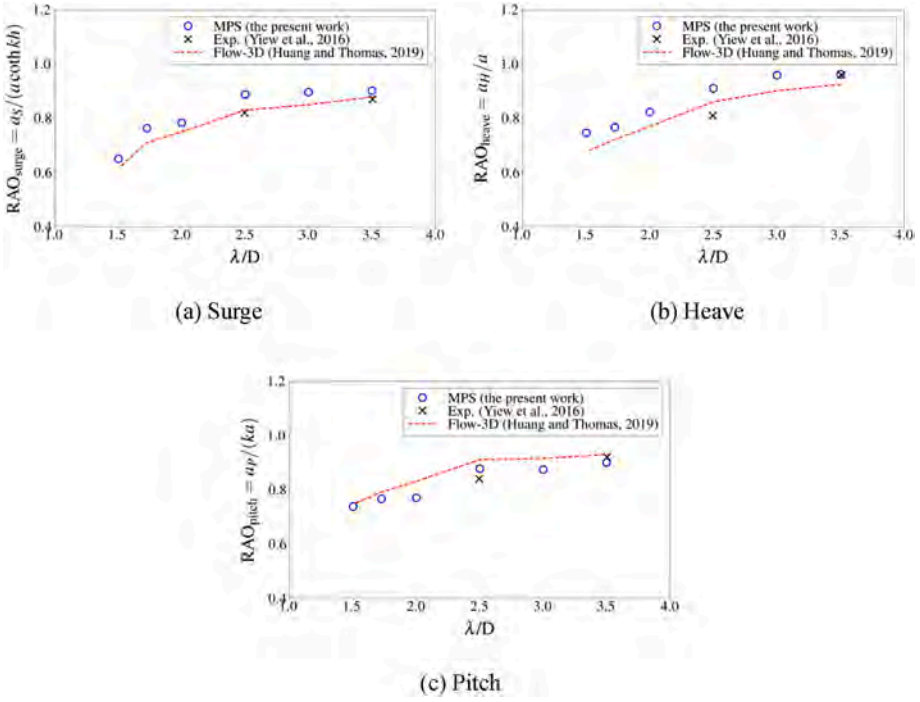

Fig. 11. Comparison of RAOs for Model 2 with an edge barrier.

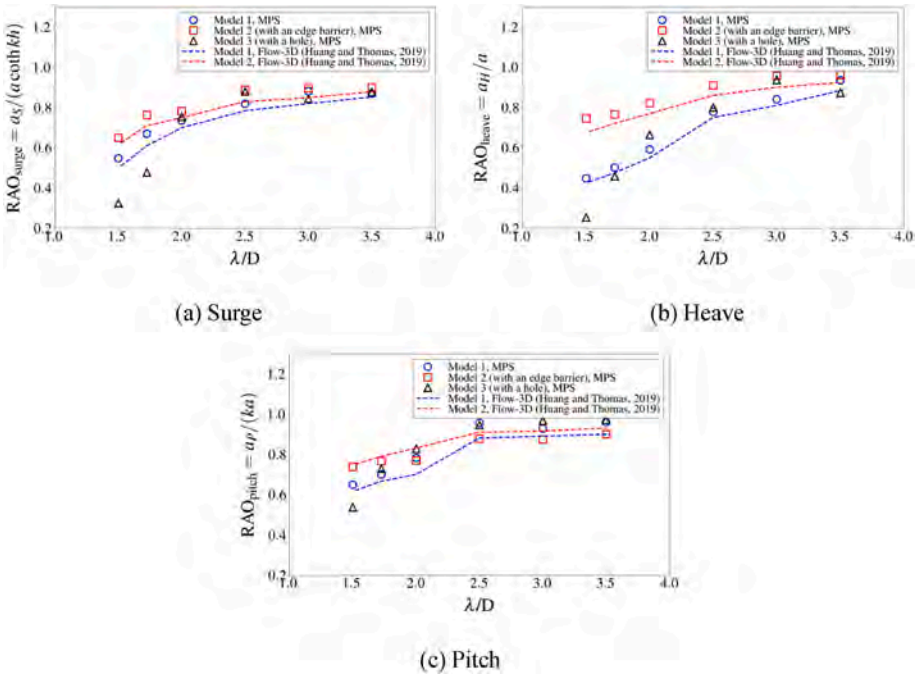

Fig. 12. Comparison of RAOs for Model 1, Model 2 and Model 3.

+0.5T are compared in which $t_0 = 4.17$ s and T is the various wave period. Note that $t = t_0$ is selected since the overwash can be obviously observed for the model 1 and model 3.

For a small wave length condition, the wave steepness is therefore great. It can be observed that overwash occurred for Model 1 without an edge barrier and much less overwash occurred for Model 2 with an edge barrier, as shown in Fig. 14(a) and (e). The heave and pitch of Model 2 are higher than that of Model 1 due to the effect of the edge barrier. For the condition with a large wave length, the wave steepness is then relatively small.

A novel type of overwash was observed for the ice model with a central hole (Model 3). For Model 3 as shown in Fig. 14(i), the ice floe is partly overwashed. On the side near the incident wave, water can flow on the upper sider of the ice, which is similar to the overwash of Model 1. The difference was made on the other side of Model 3 that the overwash waves flow over the upper side and then flow into the central hole,

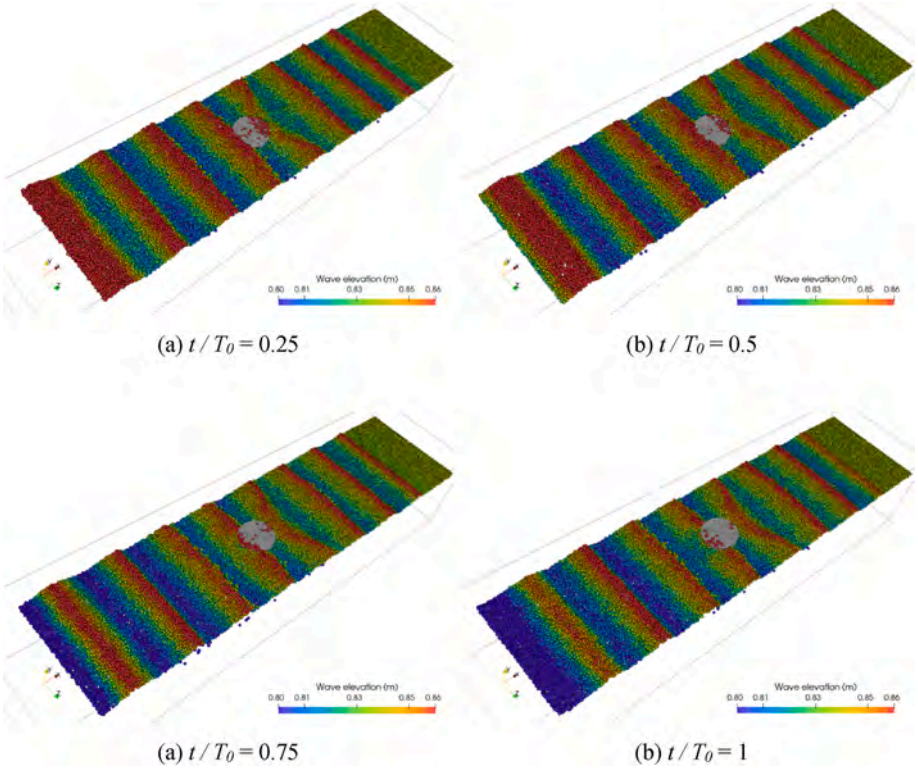

Fig. 13. Four typical instants of the free surface for Model 1 ($\lambda/D = 1.5$).

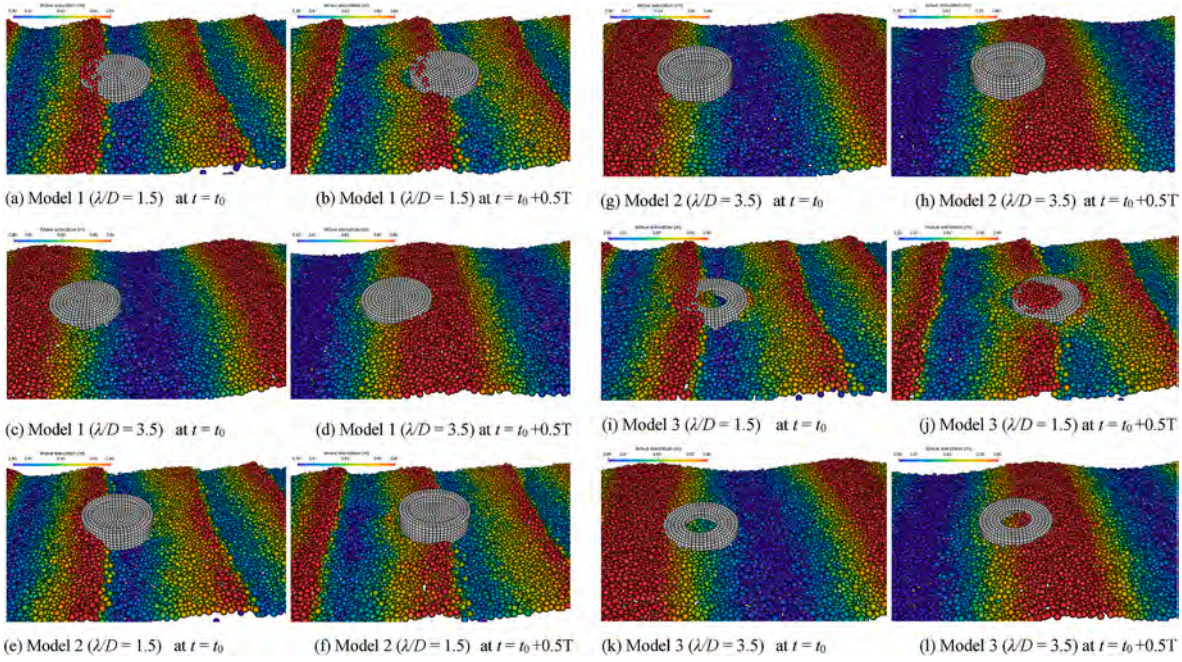

Fig. 14. Comparison of overwash with three models for various wave lengths.

interacting with the flows on the local free surface inside the ice, as shown in Fig. 14(j). The elevation of the local free surface was increased due to the incoming overwash waves. There is no overwash for all models including Model 1, Model 2 and Model 3, at the large wave length $\lambda/D = 3.5$, as shown in Fig. 14(c), (g) and (k), respectively. The heave and pitch of Model 2 and Model 3 are close to those of Model 1 in the waves with a large wave length.

The snapshots of pressure fields at selected time $t = t_0$ and $t = t_0 + 0.5T$ ($t_0 = 4.17$ s) are shown in Fig. 15. The wave crest is moving towards the ice floe at the selected time. The pressures in the fluid field are generally close for all ice floes and for different wave lengths. Furthermore, the pressure series were recorded on a point of wave flume wall ($X/D = 0, y/D = 0, z/D = 0$) and on a point of the ice floe surface ($X/D = 3.25, y/D = 2.075, z/D = 0$). Time histories of pressure for three ice floes are shown in Fig. 16. The pressures on the point of wave flume are cyclically along with the periodic motion of the wave maker. It can be observed that the amplitude of pressure oscillations for the short wave is higher than that for the long wave, despite that the average pressures are both close to 8300 Pa. The period of impact pressures on floe surface is generally equal to that of ice floe motions. It shows that overwash occurred in the short wave have negative effects on the peak value of the pressures on the ice floe surface in comparison to the long wave, in which no overwash is observed. In short wave, the peak pressure on the ice floe with an edge barrier is higher than that on the other two models,

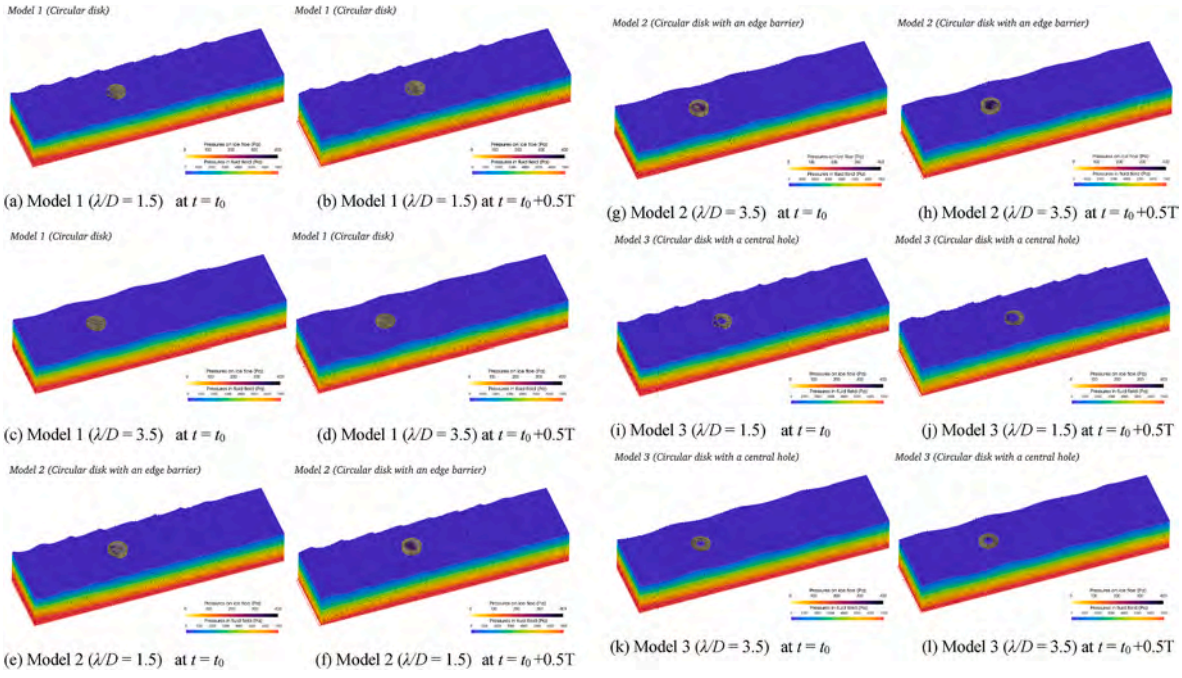

Fig. 15. Comparison of pressure fields with three models for various wave lengths.

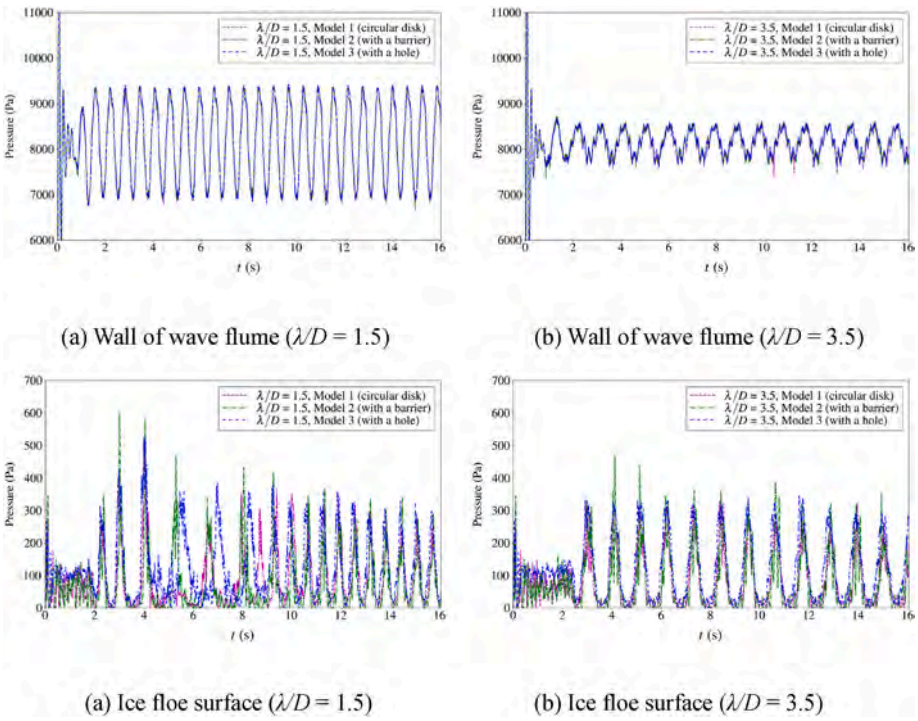

Fig. 16. Time series of pressure on a point on the wall of wave flume and on the ice floe surface.

i.e., the ice floe without a barrier and with a central hole. In addition, periods for the impact pressures are generally the same for the ice floes in long waves, since there is no overwash for all three ice floes. Different periods can be observed for the ice floes in short waves, mainly due to the effects of overwash on ice motions.

4. Conclusions

A meshfree solver based on the in-house MPS method has been employed to simulate the three-dimensional interactions between an ice floe and incident regular waves, including the process of wave overwash. The main contribution of this work is to address the effects of an edge barrier and a central hole attached to the ice floe on different sorts of overwash and wave-induced motion responses. For incident regular waves, varying wave lengths and a constant wave height are considered in numerical simulations. The results of surge, heave and pitch motions are predicted and compared with the experimental data. It can be concluded that the in-house MPS particle method has the potential to generate waves and solve the complicated free surface problems of wave-ice floe interactions with the phenomenon of overwash. The following conclusions can be drawn according to the numerical studies by applying the present meshfree solver.

1. The agreement between the results by the present IMPS method, the published numerical results by Flow-3D and the experimental data indicated the validation of the MPS method in solving the interactions between regular waves and ice floes with surge, heave and pitch motions. Compared with the mesh-based methods, the highly-deformed free surface during the overwash was well captured by using the in-house MPS method.
2. The effects of wave length on the motion responses and overwash were interpretated when the wave amplitude was kept the constant of $H/D = 0.2$. It can be concluded that the smaller the wave length was, the more frequently overwash was likely to occur. For the non-dimensional wave length λ/D from 1.5 to 2.0, the effect of overwash on the RAOs cannot be neglected. The RAOs for all models were generally less affected in long waves for λ/D greater than 2.0.
3. In short waves (large wave steepness), motion RAOs of the model with an edge barrier were larger than those of the models without an edge barrier. Since the barrier attached to the circular disk can prevent the occurrence of wave overwash, the effect of overwash can be addressed for the two models with and without an edge barrier. Wave overwash of ice floes suppressed the motion RAOs, especially for the heave motion. The wave elevation became irregular for the transmitted wave in the wave transmission region due to the effect of water overwashing the ice floe surface. In long waves, the RAOs for body motions of the models with and without an edge barrier were close since wave overwash did not occur.
4. In addition, interactions between waves and the ice floe with a hole involving the overwash were studied for the first time. Two types of overwash were observed. For the first type, the water kept flowing over the full upper surface of the ice floe (Model 1). This type has been observed commonly. The new type of overwash for Model 3 shows that the overwash waves on the upper surface can flow into the ice hole and then interacting with the local free surface inside the ice. This local interaction led to the smaller RAOs for the ice floe model with a hole than those for the other two ice floe models in short waves.

The motion analysis and the impact pressures for three ice floes in the short wave and the long wave can provide some preliminary results of the influence of the edge barrier and the central hole. Quantitative analysis will be carried out to deeply address the relation between overwash and barrier/hole in the future work.

There are several knowledge gaps including the elastic deformation of plates with different Young's modules and thicknesses. The structural deformation has an impact on the secondary peak of the vertical motion spectrum at the front edge of the plate with low rigidity (Huang et al., 2022). Challenges still remain to accurately predict the plate deformation when it is necessary to consider the air entrapment between the plate surface and free surface and air compressibility effects. There exist difficulties in the accurate prediction of overwash loads on structures during fluid-structure interactions involving wave breaking with large deformation of the free surface. The computational cost is also a

challenge to solve the detailed flow field of overwash and simulate wave transmission in an extended period time based on fully nonlinear CFD methods. However, it is still challenging for the numerical accuracy of the results obtained by meshfree methods against those by mesh-based methods. To improve the numerical accuracy, a much smaller particle spacing should also be adopted. However, it would certainly bring a high cost of both memory and time, especially for 3-D simulations. To address this problem, the present fully Lagrangian approach could be further extended to a hybrid method with a combination of the mesh method for the solutions in the far field and the meshfree method for the solutions in the near field to reduce the computational cost in future work.

CRediT authorship contribution statement

Ruosi Zha: Data curation, Writing – original draft, preparation, Visualization, Investigation, Software, Validation. **Weiwen Zhao:** Software, Data curation, Visualization, Investigation, Validation. **Decheng Wan:** Supervision, Conceptualization, Methodology, Investigation, Writing-Reviewing and Editing.

Declaration of competing interest

The authors declare that they have no known competing financial interests or personal relationships that could have appeared to influence the work reported in this paper.

Data availability

Data will be made available on request.

Acknowledgements

This work is supported by National Natural Science Foundation of China (52131102), and the National Key Research and Development Program of China (2019YFB1704200), to which the authors are most grateful.

References

Amaro, R.A., Mellado-Cusicahua, A., Shakibaeinia, A., Cheng, L.Y., 2021. A Fully Lagrangian DEM-MPS Mesh-free Model for Ice-Wave Dynamics. Cold Regions Science and Technology.
Bai, W., Zhang, T., Mcgovern, D.J., 2017. Response of small sea ice floes in regular waves: a comparison of numerical and experimental results. Ocean Eng. 129 (1), 495–506.
Bennetts, L., Williams, T., 2015. Water Wave Transmission by an Array of Floating Disks, vol. 471. Proceedings of the Royal Society A Mathematical Physical & Engineering Sciences, p. 2173.
Bennetts, L.G., Alberello, A., Meylan, M.H., Cavaliere, C., Babanin, A.V., Toffoli, A., 2015. An idealised experimental model of ocean surface wave transmission by an ice floe. Ocean Model. 96, 85–92.
Dai, M., Shen, H.H., Hopkins, M.A., Ackley, S.F., 2004. Wave rafting and the equilibrium pancake ice cover thickness. J. Geophys. Res. 109 (C7).
Hopkins, M., Shen, H.H., 2001. Simulation of pancake-ice dynamics in a wave field. Ann. Glaciol. 33, 355–360.
Huang, L., Thomas, G., 2019. Simulation of wave interaction with a circular ice floe. J. Offshore Mech. Arctic Eng. 141 (4), 041302.1-041302.9.
Huang, L., Ren, K., Li, M., Tuković, Željko, Cardiff, P., Thomas, G., 2019. Fluid-structure interaction of a large ice sheet in waves. Ocean Eng. 182, 102–111.
Huang, L., Lu, W., Yang, J., Dong, Q., 2022. Experimental study on surface waves around a novel model of ice floe. Cold Reg. Sci. Technol. 193, 2103380.
Kohout, A.L., Williams, M.J.M., Dean, S.M., Meylan, M.H., 2014. Storm-induced sea-ice breakup and the implications for ice extent. Nature 509, 604–607.
Lee, B.H., Park, J.C., Kim, M.H., Hwang, S.C., 2011. Step-by-step improvement of MPS method in simulating violent free-surface motions and impact-loads. Comput. Methods Appl. Mech. Eng. 200 (9–12), 1113–1125.
Koshizuka, S., Oka, Y., 1996. Moving-particle semi-implicit method for fragmentation of incompressible fluid. Nucl. Sci. Eng 123, 421–434..
Lee, C.M., Cole, S., Doble, M., Freitag, L., Hwang, P., Jayne, S., Jeffries, M., Krishfield, R., Maksym, T., Maslowski, W., 2012. Marginal Ice Zone (MIZ) Program: Science and Experiment Plan. Washington Univ. Seattle Applied Physics Laboratory. Report No. APL-UW-1201.
Li, A., Fang, H., Liu, Y., 2022. Hydroelastic analysis of interaction between water waves and a floating laminated disk. Phys. Fluids 34 (4).
Luo, M., Khayyer, A., Lin, P., 2021. Particle methods in ocean and coastal engineering. Appl. Ocean Res. 114, 102734.
Marquart, R., Bogaers, A., Skatulla, S., Alberello, A., Toffoli, A., Nisters, C., Vichi, M., 2021. A computational fluid dynamics model for the small-scale dynamics of wave, ice floe and interstitial grease ice interaction. Fluid 6 (5), 176.
Martin, S., Becker, P., 1987. High-frequency ice floe collisions in the Greenland sea during the 1984 Marginal Ice Zone experiment. J. Geophys. Res.: Oceans 92 (C7), 7071–7084.
Massom, R.A., Stammerjohn, S.E., 2010. Antarctic sea ice change and variability - physical and ecological implications. Polar Science 4 (2), 149–186.
Matias, A., Williams, Jon J., Masselink, G., Ferreira, Ó., 2012. Overwash threshold for gravel barriers. Coast Eng. 63, 48–61.
McGovern, D.J., Bai, W., 2014. Experimental study of wave-driven impact of sea ice floes on a circular cylinder. Cold Reg. Sci. Technol. 108, 36–48.
Meylan, M., Squire, V.A., 1994. The response of ice floes to ocean waves. J. Geophys. Res. Oceans 99. C1.
Meylan, M.H., Yiew, L.J., Bennetts, L.G., French, B.J., Thomas, G.A., 2015. Surge motion of an ice floe in waves: comparison of a theoretical and an experimental model. Ann. Glaciol. 56 (69), 155–159.
Montiel, F., Bonnefoy, F., Ferrant, P., Bennetts, L.G., Squire, V.A., Marsault, P., 2013a. Hydroelastic response of floating elastic discs to regular waves. Part 1. Wave basin experiments. J. Fluid Mech. 723, 604–628.
Montiel, F., Bennetts, L.G., Squire, V.A., Bonnefoy, F., Ferrant, P., 2013b. Hydroelastic response of floating elastic discs to regular waves. Part 2. Modal analysis. J. Fluid Mech. 723, 629–652.
Montiel, F., Squire, V., Bennetts, L., 2016. Attenuation and directional spreading of ocean wave spectra in the Marginal Ice Zone. J. Fluid Mech. 790, 492–522.
Nelli, F., Bennetts, L.G., Skene, D.M., Monty, J.P., Lee, J.H., Meylan, M.H., Toffoli, A., 2017. Reflection and transmission of regular water waves by a thin, floating plate. Wave Motion 70, 209–221.
Nelli, F., Bennetts, L., Sken, D., Toffoli, A., 2020. "Water wave transmission and energy dissipation by a floating plate in the presence of overwash,". J. Fluid Mech. 889.
Ni, B., Pan, Y., Yuan, G., Xue, Y., 2021. An experimental study on the interaction between a bubble and an ice floe with a hole. Cold Reg. Sci. Technol. 187 (2), 103281.
Orzech, M.D., Shi, F., Veeramony, J., Bateman, S., Calantoni, J., Kirby, J.T., 2016. Incorporating floating surface objects into a fully dispersive surface wave model. Ocean Model. 102, 14–26.
Pak, C.J., Han, P.N., Ri, K.C., Ri, Y.K., Hwang, I.C., 2021. Numerical analysis of the nonlinear free surface flow around an advancing ship using moving particle semi-implicit method. AIP Adv. 11 (3), 035106.
Pitt, J.P.A., Bennetts, Luke G., Meylan, Michael H., Massom, Robert A., Toffoli, A., 2022. Model predictions of wave overwash extent into the marginal ice zone. J. Geophys. Res.: Oceans 127 (10), e2022JC018707.
Rosetti, G.F., Pinto, M.L., De Mello, P.C., Sampaio, C.M.P., Simos, A.N., Silva, D.F.C., 2019. CFD and experimental assessment of green water events on an FPSO hull section in beam waves. Mar. Struct. 65, 154–180.
Shen, Z., Wan, D., 2013. RANS computations of added resistance and motions of a ship in head waves. Int. J. Offshore Polar Eng. 23 (4), 263–271.
Shen, Z., Carrica, P.M., Wan, D., 2014. Ship motions of KCS in head waves with rotating propeller using overset grid method. In: Proceedings of the ASME 33rd International Conference on Ocean. Offshore and Arctic Engineering, San Francisco, USA. June.
Skene, S.D., Bennetts, L., Meylan, M., Toffoli, A., Monty, J., 2015a. Modelling Water Wave Overwash of a Sea Ice Floe. International Workshop on Water Waves & Floating Bodies.
Skene, D., Bennetts, L., Meylan, M., Toffoli, A., 2015b. Modelling water wave overwash of a thin floating plate. J. Fluid Mech. 777, R3.
Skene, D., Bennetts, L., Wright, M., Meylan, M., Maki, K., 2018. Water wave overwash of a step. J. Fluid Mech. 839, 293–312.
Squire, V.A., 2020. Ocean wave interactions with sea ice: a reappraisal. Annu. Rev. Fluid Mech. 52 (1).
Teng, Y., Tan, H., Kim, J., Jang, H., Tcherniguin, N., 2020. Methodology of Simulating Spread-Moored FPSO Green Water Using CFD-Based Numerical Wave Basin. Offshore Technology Conference Asia.
Thomson, J., Rogers, W.E., 2014. Swell and sea in the emerging arctic ocean. Geophys. Res. Lett. 41 (9), 3136–3140.
Thomson, J., Squire, V., Ackley, S., Rogers, E., Babanin, A., Guest, P., Maksym, T., Wadhams, P., Stammerjohn, S., Fairall, C., 2013. "Sea State and Boundary Layer Physics of the Emerging Arctic Ocean,". Washington Univ Seattle Applied Physics Laboratory. Report No. APL-UW-1306.
Toffoli, A., Bennetts, L.G., Meylan, M.H., Cavaliere, C., Alberello, A., Elsnab, J., Monty, J. P., 2015. Sea ice floes dissipate the energy of steep ocean waves. Geophys. Res. Lett. 42 (20), 8547–8554.
Tran-Duc, T., Meylan, M.H., Thamwattana, N., Lamichhane, B.P., 2020. Wave interaction and overwash with a flexible plate by Smoothed Particle Hydrodynamics. Water 12 (12), 3354.
Tran-Duc, T., Meylan, Michael H., Thamwattana, N., 2023. Smoothed particle hydrodynamics simulations for wave induced ice floe melting. Phys. Fluids 35 (4).
Xie, F., Zhao, W., Wan, D., 2022. Overview of moving particle semi-implicit techniques for hydrodynamic problems in ocean engineering. J. Mar. Sci. Appl. 21 (3), 1–22.
Yiew, L., Bennetts, L., Meylan, M., French, B., Thomas, G., 2016. Hydrodynamic responses of a thin floating disk to regular waves. Ocean Model. 97, 52–64.
Zhang, Y., Wan, D., 2017. Numerical study of interactions between waves and free rolling body by IMPS method. Comput. Fluids 155, 124–133.
Zhang, Y., Wan, D., 2018. MPS-FEM coupled method for sloshing flows in an elastic tank. Ocean Eng. 152, 416–427.

Zhang, Y., Wan, D., Hino, T., 2014. Comparative study of MPS method and level-set method for sloshing flows. J. Hydrodyn. Ser. B. 4 (26), 85–93.
Zhang, L., Lin, S., Wang, C., Xie, D., Sun, J., 2019a. A new simulation model for hydrodynamic behavior of rigid body in narrow space. Ocean Eng. 182, 427–441.
Zhang, N., Zheng, X., Ma, Q., 2019b. Study on wave-induced kinematic responses and flexures of ice floe by Smoothed Particle Hydrodynamics. Comput. Fluid 189, 46–59.
Zhang, G., Chen, X., Wan, D., 2019c. MPS-FEM coupled method for study of wave-structure interaction. J. Mar. Sci. Eng. 18 (11).